High-pressure and magnetism in the quasi-one-dimensional solid solution Ca1-xNaxCr2O4: A multimodal neutron, muon, and x-ray study

High-pressure and magnetism in the quasi-one-dimensional solid solution $Ca_{1-x}Na_xCr_2O_4$: A multimodal neutron, muon, and x-ray study

E. Nocerino,[1,2,*] H. Sakurai,[3] O. K. Forslund,[4,5] K. Papadopoulos,[6] D. J. Mukkattukavil,[7] D. Andreica,[8] G. Simutis,[9] R. Khasanov,[9] N. Ishimatsu,[10] N. Kawamura,[11] C. L. Bull,[12,13] N. P. Funnell,[12] J. Sugiyama,[14] I. Umegaki,[15] Y. Sassa,[2] and M. Månsson[2,†]

[1]*Department of Chemistry, Stockholm University, SE-10691 Stockholm, Sweden*
[2]*Department of Applied Physics, KTH Royal Institute of Technology, SE-106 91 Stockholm, Sweden*
[3]*National Institute for Materials Science, Namiki, Tsukuba, Ibaraki 305-0044, Japan*
[4]*Physik-Institut, Universität Zürich, Winterthurerstrasse 190, CH-8057 Zürich, Switzerland*
[5]*Department of Physics and Astronomy, Uppsala University, Box 516, SE-75120 Uppsala, Sweden*
[6]*Department of Physics, Chalmers University of Technology, SE-412 96 Göteborg, Sweden*
[7]*Department of Physics and Astronomy, Uppsala University, Box 516, SE-751 20 Uppsala, Sweden*
[8]*Faculty of Physics, Babes-Bolyai University, 3400 Cluj-Napoca, Romania*
[9]*PSI Center for Neutron and Muon Sciences CNM, 5232 Villigen PSI, Switzerland*
[10]*Geodynamics Research Center, PIAS, Ehime University, Matsuyama 790-8577, Japan*
[11]*Japan Synchrotron Radiation Research Institute, SPring-8, 1-1-1 Kouto, Sayo, Hyogo 679-5198, Japan*
[12]*ISIS Neutron and Muon Source, Rutherford Appleton Laboratory, Didcot OX11 0QX, United kingdom*
[13]*EaSTChem School of Chemistry, The University of Edinburgh, King's Buildings, West Mains Road, Edinburgh EH9 3FJ, United kingdom*
[14]*Neutron Science and Technology Center, Comprehensive Research Organization for Science and Society (CROSS), Tokai, Ibaraki 319-1106, Japan*
[15]*Muon Science Laboratory, Institute of Materials Structure Science, KEK, Tokai, Ibaraki 319-1106, Japan*

(Received 5 May 2025; revised 20 January 2026; accepted 3 February 2026; published 10 March 2026)

We investigate the pressure-dependent magnetism of the quasi-one-dimensional solid solution $Ca_{1-x}Na_xCr_2O_4$ using neutron diffraction, Cr K-edge x-ray absorption spectroscopy, and muon spin rotation/relaxation. Na substitution is known to increase oxygen-ligand hole density (partial Cr^{3+} to Cr^{4+} character) and to drive the evolution from incommensurate order in $CaCr_2O_4$ to commensurate antiferromagnetism in $NaCr_2O_4$, suggesting a complex interplay between charge doping and structural changes. Here we apply hydrostatic pressure to tune the lattice without altering the nominal hole count, thereby separating compression effects from ligand-hole physics. For $x = 0$ and $x = 0.5$ the magnetic transition temperature is essentially pressure independent within our explored range, whereas in $NaCr_2O_4$ long-range order is progressively suppressed with pressure, as seen by a decrease of T_N and of the magnetic Bragg intensity. Over the same pressure range, Cr K-edge x-ray absorption spectroscopy shows no resolvable change in the average Cr valence or coordination, and the refined corner-sharing Cr–O–Cr geometry remains nearly invariant within uncertainty. Extrapolating the pressure dependence of the magnetic order parameter suggests a critical pressure $P_c = 107(8)$ kbar for complete suppression of long-range order. These results support ligand-hole density as the primary control parameter across $Ca_{1-x}Na_xCr_2O_4$, with pressure acting as a secondary electronic tuning knob that weakens ordering in the Na-rich end member without inducing a new magnetic phase.

DOI: 10.1103/gpc2-fxmj

I. INTRODUCTION

The peculiar physical properties of low-dimensional systems have attracted considerable interest in condensed-matter physics for several decades. Indeed, in structurally one-dimensional (1D) and quasi-one-dimensional (Q1D) metals, the electron system, described as a Fermi liquid in higher-dimensional lattices, is better described with a Luttinger-liquid model, where the low-lying excited states in a 1D electron gas are expressed in terms of bosons [1–4]. In this kind of systems unconventional noncollinear magnetic ground states are often realized due to the spatial constraints of their low-dimensional lattice and the complex network of competing magnetic interactions between nearest- and next-nearest-neighbor spins [5–12]. Beyond the clear fundamental interest inspired by these materials, they are also pivotal in the development of quantum devices [13–15] and in the design of

*Contact author: elisabetta.nocerino@su.se
†Contact author: condmat@kth.se

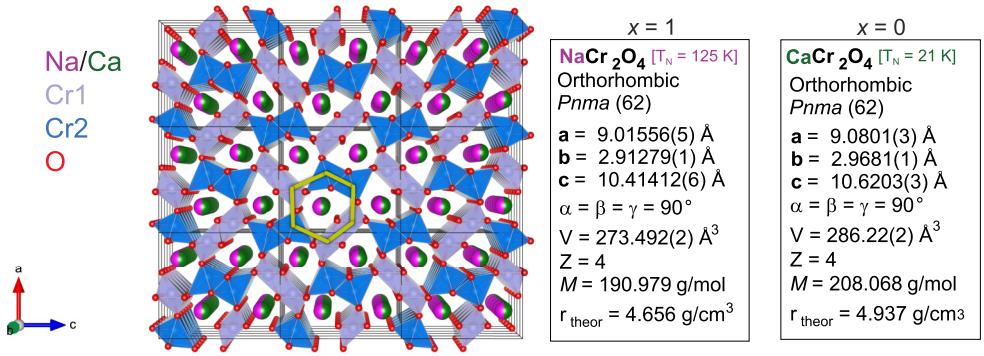

FIG. 1. Crystal structure of Na/$CaCr_2O_4$ seen from the *ac* plane and unit-cell parameters for $NaCr_2O_4$ [37] and $CaCr_2O_4$ [10]. The distorted hexagonal channel that lodges the Ca^{2+} and Na^{+} ions is evidenced in yellow.

the next generation battery materials with highly anisotropic ion diffusion paths [16–21], leading quantum physics into practical applications.

By virtue of the competitive magnetic couplings that determine the magnetic order in low–dimensional materials, it is not trivial to predict the ground state that they will develop. Compounds with similar crystal structures can, indeed, manifest a very varied magnetic phenomenology [22–26]. Pressure-induced structural modifications often prove to be very effective in driving major changes in the magnetic landscape of Q1D material [27–29]. Strain is therefore considered one of the possible tuning parameters for magnetic exchange interactions, together with chemical doping. This work presents the results of a systematic pressure-dependent study on the solid solution between the Q1D calcium-ferrite type compounds $CaCr_2O_4$ and $NaCr_2O_4$, i.e., $Ca_{1-x}Na_xCr_2O_4$, carried out by neutron diffraction (ND), x-ray absorption spectroscopy (XAS) and muon spin rotation/relaxation (μ^+SR). The structure of calcium-ferrites, based on the prototypical compound $CaFe_2O_4$, exhibit a peculiar geometrically frustrated lattice, in which a network of triangular (or zigzag) magnetic ladders form a honeycomb-like mesh, which lends itself very well to the occurrence of competing magnetic interactions, resulting in a wide variety of exotic ground states [30–34].

$Ca_{1-x}Na_xCr_2O_4$ [35] is isostructural to β-$CaCr_2O_4$ [$x = 0$] and $NaCr_2O_4$ [$x = 1$]. Both these compounds have a calcium-ferrite structure (also called postspinel [36]) with orthorhombic space group *Pnma*, in which Cr ions occupy two distinct crystallographic positions (labelled as "Cr1" and "Cr2" in Fig. 1). Here double chains of CrO_6 edge-sharing octahedra form the aforementioned honeycomb-like network where Ca^{2+} and Na^{+} ions are located. The anisotropic arrangement of these chains defines channel-like cavities, whose pattern evokes a distorted hexagonal motif, motivating the classification of these materials as Q1D (Fig. 1).

β-$CaCr_2O_4$ was found to possess an incommensurate $S = 3/2$ antiferromagnetic structure (transition at $T_N = 21$ K), in which the magnetic moments of Cr^{3+} ions are arranged in double cycloidal chains with opposite chirality along the zigzag ladder. This peculiar spin arrangement is suggested to be originated from a combination of symmetric and antisymmetric exchange interaction terms [10].

In $NaCr_2O_4$, the Cr is found in the uncommon mixed valence state Cr^{3+}/Cr^{4+} [38], which requires high-pressure synthesis for structural stabilization, unlike its pure Ca counterpart [39]. This unusual condition is believed to be at the origin of many of the physical properties of this material, namely Cr orbital ordering [40], anomalous colossal magnetoresistance CMR [39], and atypical coexistence of positive and negative charge transfer states [38], leading to a $3d^3\,\underline{L}$ charge ordering configurations for the Cr^{4+} $3d^2$ electronic states [41]. In this configuration, ligand holes are delocalized over the Cr–O–Cr network, with the hole density primarily focused at the corner-sharing oxygen sites [40]. Systematic studies across the solid solution $Ca_{1-x}Na_xCr_2O_4$ have shown that increasing Na content enhances the oxygen-ligand hole density and drives the system deeper into the negative charge-transfer regime [35,38,42]. This increase in ligand-hole density has been directly linked to the evolution of magnetic interactions via double-exchange pathways and to the emergence of commensurate AFM (C-AFM) order in the Na-rich compound. In our recent neutron diffraction study, the magnetic ground state of $NaCr_2O_4$ was found to be C-AFM with FM coupling of the Cr moments in double rutile chains antiferromagnetically coupled in the honeycomb-like plane ($T_N = 125$ K) [37]. The Cr ordered moments were found to have a canting angle and a magnitude of about 4.3 μB per Cr, which is significantly larger than expected from a simple average of Cr^{3+} ($S = 3/2$) and Cr^{4+} ($S = 1$) ions [37]. This discrepancy reflects the role of ligand holes, which prevent a static Cr^{3+}/Cr^{4+} charge ordering (that would otherwise be expected) and instead relieve charge frustration through dynamic hole hopping across Cr–O–Cr bonds [38,41]. The resulting double-exchange–like mechanism stabilizes high-spin Cr sites with effective Cr^{2+}-like d^4 character ($S = 2$), thereby reconciling the large ordered moment with the mixed-valence electronic configuration. Importantly, the $S = 2$ description should be understood as an effective spin state, arising from ligand-hole stabilization rather than from a literal Cr^{2+} ionic species. Recent theoretical calculations further support this interpretation, predicting spin disproportionation between the crystallographically distinct Cr1 and Cr2 sites [42].

Therefore, while in β-$CaCr_2O_4$ the magnetic couplings are established along the frustrated ladders of Cr, in $NaCr_2O_4$ the magnetic interactions "escape" the Q1D Cr chains and realize

a 2D magnetic structure with alternating arrangement of FM rutile chains. These two conditions are remarkably divergent considering the structural similarity of the two materials.

Here the main differences between β-$CaCr_2O_4$ and $NaCr_2O_4$ are the unit-cell volume, which is bigger for β-$CaCr_2O_4$, owing to the larger atomic radius of the Ca element, and the valence state in which the Cr ions are found (Cr^{3+} in β-$CaCr_2O_4$ and mixed Cr^{3+}/Cr^{4+} in $NaCr_2O_4$). Therefore, the tuning parameters that leads the magnetic ground state in the solid solution $Ca_{1-x}Na_xCr_2O_4$ from IC-AFM, in the $[x = 0]$ member, to C-AFM, in the $[x = 1]$ member, are either the Cr-Cr distances in the crystal lattice or the density of the ligand holes in the oxygen sites. Given the established role of ligand-hole density in tuning magnetism, the key question addressed in the present study is whether external pressure—which compresses the lattice but does not alter the nominal hole count—can induce effects comparable to Na substitution or whether ligand-hole density remains the decisive control parameter.

In this work, we show that the hydrostatic compression affecting Cr-Cr distances in this system induces no significant changes in the electronic structure of $NaCr_2O_4$, as evidenced by XAS measurements, while it is responsible for suppressing the magnetic order, as observed by neutron diffraction. Pressure does not seem to affect the other members of the solid solution with $[x = 0]$ and $[x = 0.5]$ (as for μ^+SR measurements), revealing that the hole density of the Cr chains is the dominant tuning parameter for the determination of the magnetic order in these materials and that the coupling mechanisms here established are not sensitive to variations in the Cr-Cr distances alone.

II. EXPERIMENTAL SETUP

Polycrystalline samples of $Ca_{0.5}Na_{0.5}Cr_2O_4$ were prepared from a stoichiometric mixture of CaO, $NaCrO_2$, Cr_2O_3, and CrO_3 at 1300°C under a pressure of 6 GPa, while the $NaCr_2O_4$ was prepared under a pressure of 7 GPa.

Samples of β-$CaCr_2O_4$ were prepared, instead, by a solid-state reaction of a stoichiometric mixture of $CaCO_3$ and Cr_2O_3 at 1300°C, under ambient pressure, for 12 h in an Ar gas flow. For further details on the synthesis of these samples refer to Ref. [35].

All samples were confirmed to be predominantly single-phase with a $CaFe_2O_4$-type *Pnma* structure, as determined by powder x-ray diffraction (XRD) analyses. Minor impurities, potentially including Cr_2O_3 may be present but are below the detection limit and do not affect the reported measurements.

All images involving crystal structure were made with the VESTA software [43], the temperature- and pressure-dependent plots and fitting are produced with the software IGORPRO [44] and the software MATLAB [45].

A. The μ^+SR experiment

The μ^+SR spectra at ambient pressure have been acquired, as a function of temperature, at the multipurpose surface muon instrument Dolly [46], while the spectra under pressure (ranging between 10 and 30 kbar) have been acquired, as a function of temperature, at the general purpose decay channel spectrometer GPD [47]. Both these beamlines are located at the Paul Scherrer Institute (PSI) in Switzerland [48].

For the measurements in Dolly, ∼200 mg of sample in powder was encapsulated in a 1×1 cm^2 area aluminum-coated Mylar tape (0.05 mm thickness) in order to reduce the background signal. This envelope was attached to a low background sample holder inserted in a helium exchange gas cryostat [49] (temperature range 1.6 K to 300 K). To avoid history-dependent effects, all the measurements were performed following a zero-field cooling protocol, i.e., the samples were cooled to the measurement temperature in the absence of any applied field.

For the GPD measurements the sample was compressed in a 2-mm thickness, 5.9-mm diameter pellet and pushed into a piston-cylinder pressure cell (Fig. 2) made of Cu-Be for the inner wall and of MP35 alloys for the outer wall [50,51]. Daphne oil was used as hydrostatic pressure medium. The applied pressure was determined using the superconducting transition temperature of an indium wire placed inside the cell. A short susceptibility scan was performed once at each applied pressure point prior to the μ^+SR measurements, after which the pressure value was assumed stable for the duration of the run. This procedure, standard at PSI for piston-cylinder pressure cells, avoids repeated thermal cycling of the sample during beam time. The cell was screwed on top of a low background sample holder, inserted in a ^{4}He vaporizer cryostat [52] (temperature range: 2.5 K to 300 K).

Figure 2 displays a pictorial representation of the sample mounting in the pressure cell. The muon stopping profile in the sample is Gaussian, so it is not possible to prevent the muons in the tails of the distribution from being implanted in the pressure cell. Since the cell is made of Cu-Be (that is a nonmagnetic alloy) this does not compromise the results, nevertheless a static Kubo-Toyabe relaxation component in the muon polarization function will be added to the zero-field (ZF) spectra, due to the muons stopping in the cell (see Sec. III). Hence, in order to keep the mean value of the muon beam distribution in the center of the sample, a muon momentum scan and vertical sample position scans were performed before each initial sample setup. The μ^+SR data were fitted using the software package *MUSRFIT* [53].

B. The neutron diffraction experiment

The neutron diffraction patterns were collected, as a function of pressure, at the time-of-flight high-flux diffractometer PEARL, ISIS Neutron and Muon Facility (UK) [54]. About 400 mg of $NaCr_2O_4$ powder was loaded into a null-scattering Ti-Zr alloy capsule gasket [55] in a Paris-Edinburgh (P-E) press. A uniform hydrostatic pressure was applied up to 43 kbar, in steps of about 6 kbar, through a perdeuterated methanol:ethanol (4:1 by volume) mixture as pressure medium and maintained by means of a computer-controlled hydraulic system. Together with the sample, a lead pellet was also included in the gasket assembly as a pressure calibrant. The applied pressure was estimated from the refined lattice parameters of the lead pellet using its well-established equation of state. We note that, unlike in the μ^+SR experiment, the superconducting transition of lead was not used for calibration in this case. The temperature-dependent

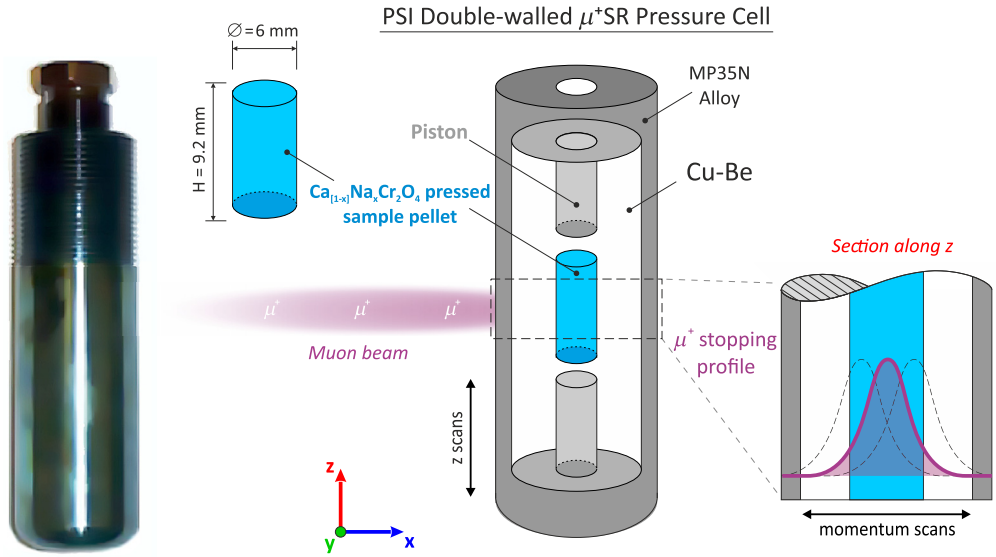

FIG. 2. Photograph and schematic representations of the double-walled MP35N and Cu-Be pressure cell used for μ^+SR measurements at the GPD beamline. The arrangement of stacked sample pellets is illustrated in cyan. An illustration of muon momentum scans, optimized to enhance the sample signal and suppress background from the pressure cell, is also shown. Figure adapted with permission from Ref. [27].

measurements were performed in the range [100–300] K by partially immersing the press in a liquid-nitrogen-filled tank.

The diffracted neutrons were collected in two set of detectors: the transverse bank, normal to the incoming beam with an angle coverage of $81.2^\circ < 2\theta < 98.8^\circ$, and the longitudinal bank, accessible by rotating the cell 90° with respect to the beam, which covers the back-scattering angular range $100^\circ < 2\theta < 160^\circ$ and a low angle range $20^\circ < 2\theta < 60^\circ$. The data from the transverse bank were used mainly for pressure determination, while the longitudinal bank allowed the observation of magnetic peaks due to its high-d (low-Q) range coverage. The data reduction has been performed with the software MANTID [56].

C. The XAS experiment

The x-ray absorption spectroscopy experiment was carried out at the hard x-ray high-pressure beamline BL39XU in SPring-8 (Japan) [57]. XAS spectra at the Cr K edge (x-ray energy range: [5.9–6.5] keV) were collected for the stoichiometric $NaCr_2O_4$ (in powder), at $T = 300$ K, under pressures between ambient and a maximum of 124 kbar using a diamond anvil cell (DAC) provided on site [58]. For some selected pressure points (124, 45, 20, 3) kbar a temperature scan in the temperature range 10 K to 300 K has also been performed. High pressure was applied with nanopolycrystalline diamond anvil (NPD) to avoid strong x-ray diffraction from diamonds [59,60]. In addition, hole-fabricated anvil was used for one of NPDs to suppress large x-ray absorption of the anvil at the Cr K edge. Si 220 double-crystal monochromator and Rh-coated mirror was used for high-energy resolution measurements. A Kirkpatrick and Baez mirror for high-pressure measurements was also used to focus micro-beam x rays. Ar fluid was loaded to the DAC as a pressure-transmitting medium. For low-temperature measurements, a pulse-tube-type cryostat was used. The data normalization has been performed using the software ATHENA [61].

III. RESULTS AND DISCUSSION

In the following section, the experimental results with the related data analysis are collected. In the first subsection the μ^+SR results at ambient pressure and under applied pressure for different temperatures are described. The measurements at ambient pressure were intended to confirm the previous findings and constitute the reference point for the measurements under pressure. In the second and third subsections the ND and XAS results under applied pressure are described, respectively.

A. μ^+SR results

1. ZF-μ^+SR results

A ZF μ^+SR experiment has been carried out for different temperatures, in ambient pressure, on the three members of the solid solution $Ca_{1-x}Na_xCr_2O_4$ with $[x = 0, 0.5, 1]$ in order to observe the evolution of the implanted muons' spin polarization, which is related to the sample's internal magnetic field distribution. The resulting ZF spectra at base temperature $T = 2$ K are displayed in Fig. 3, with their respective best fit curves (shown as continuous lines).

Here the clear oscillations visible in the asymmetries for all the three samples are linked to the muons spin's Larmor precession whose angular frequency (ω) that changes according to the local magnetic field (of modulus B) detected by the probe particle allows us to determine the magnetic field intensity distribution in the sample, through the direct proportionality relation $\omega = \gamma_\mu B$ (where $\frac{\gamma_\mu}{2\pi} = 13.55342[\frac{\text{kHz}}{\text{Oe}}]$ is the muon gyromagnetic ratio). The time dependence of the muon spin polarization can be described, for all the spectra in this plot, by exponentially relaxing oscillating functions. Specifically, the fit function chosen for $CaCr_2O_4$ $[x = 0]$ is

$$A_0 P_{ZF}(t) = A_{SDW} J_0\left(2\pi \nu_{SDW} t + \frac{\pi\phi}{180}\right) \cdot e^{(-\lambda_{SDW} t)} + A_{tail} \cdot e^{(-\lambda_{tail} t)}, \quad (1)$$

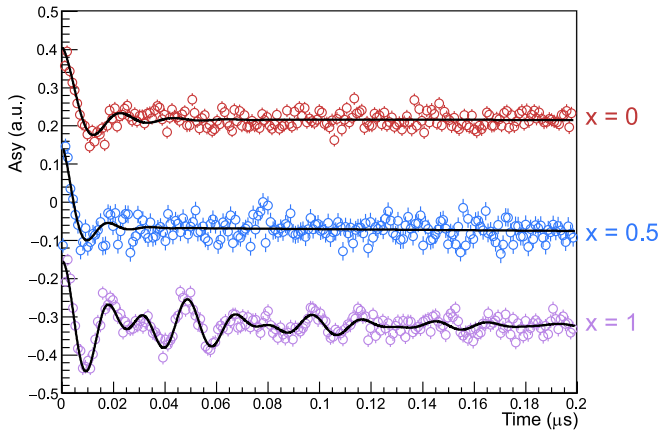

FIG. 3. Early-time-domain μ^+SR spectra in zero field at $T = 2$ K for $CaCr_2O_4$ (red data), $Ca_{0.5}Na_{0.5}Cr_2O_4$ (blue data), and $NaCr_2O_4$ (violet data). For clarity of display, these spectra are shifted along the y axis. The continuous lines are fits to the functions described in the main text.

where A_0 is the initial asymmetry, P_{ZF} is the muon spin polarization function, $J_0(2\pi\nu_{SDW}t + \frac{\pi\phi}{180})$ is the Bessel function of the first kind of order 0, ν_{SDW} is the frequency of the Larmor precession, ϕ is the initial phase in degrees (in the case of this specific data set $\phi = 0$), λ_{SDW} is an additional exponential relaxation rate associated to the Bessel function, and $A_{tail} \cdot e^{(-\lambda_{tail}t)}$ is a nonoscillatory exponential tail term arising from muons experiencing internal magnetic fields that are aligned (i.e., parallel) with their initial spin polarization. These parallel components do not induce precession. The fast relaxing oscillation in the asymmetry of $CaCr_2O_4$ reveals the existence of a wide distribution of intensities for the static magnetic field at the muon sites. Additionally, the Bessel function is commonly used to describe the muon spin precession in a magnetic environment created by a single $\boldsymbol{k}$-vector incommensurate spin-density wave [62–64]. This is consistent with the occurrence of an incommensurate spin ordering, as expected from previous results obtained by ND [10].

The fit function chosen for the $Ca_{0.5}Na_{0.5}Cr_2O_4$ $[x = 0.5]$ is analogous to the one used for $CaCr_2O_4$ [Eq. (1)].

Here attempts to include additional oscillating components to the terms already defined for Eq. (1) did not improve the fit, and therefore they were disregarded. This behavior of the muon spin polarization suggests that the Na doping up to $[x = 0.5]$ is not enough to significantly modify the nature of the magnetic ground state in $Ca_{1-x}Na_xCr_2O_4$, which remains in the form of an incommensurate spin-density wave. This observation contrasts with earlier reports based on bulk magnetometry that suggested spin-glass-like behavior in the same doping range [35].

Our μ^+SR data, sensitive to local static fields, show no evidence for spin-glass freezing within the available sensitivity and statistics. In particular, the spectra are better described by critically damped oscillations rather than by nonoscillatory or stretched-exponential relaxation. The weak transverse field (wTF)-μ^+SR asymmetry exhibit a recovery across T_N that is consistent with a second-order transition into long-range magnetic order within an inhomogeneous local field environment rather than with the anomalously broad or incomplete recovery characteristic of glassy freezing. These observations, together with earlier reports of incommensurate or commensurate antiferromagnetic order in $Ca_{1-x}Na_xCr_2O_4$ [10,37], support the persistence of coherent magnetic ordering. Of course, a more direct proof of the ordering wave vector and its persistence would require complementary high-resolution neutron diffraction measurements. Within the framework of the present study, the most notable difference between $CaCr_2O_4$ and $Ca_{0.5}Na_{0.5}Cr_2O_4$ is the sharp increase in the muon precession frequency, which goes from 35(1) to 61(6) MHz. Given the relationship of direct proportionality between the muon spin precession frequency and the intensity of the local magnetic field at the muon sites, the increase in ω reflects an increase in the mean value of the static internal field modulus. This is qualitatively consistent with an enhancement of the value of the Cr magnetic moment, as expected from previous studies [10,37].

While we attribute the increase in muon precession frequency from ∼35 MHz ($CaCr_2O_4$) to ∼61 MHz ($Ca_{0.5}Na_{0.5}Cr_2O_4$) primarily to the enhanced ordered Cr moments, we note that the absolute precession frequency is determined by the local internal magnetic field at the muon stopping site. In principle, changes in the muon stopping site or subtle modifications of the local electrostatic and magnetic environment could also contribute to the observed frequency shift. However, all compositions studied here crystallize in the same orthorhombic structure, and no structural transitions that would significantly alter the muon stopping positions are known across the solid solution, as also confirmed by muon sites calculations [21]. Moreover, the systematic correlation between the higher precession frequencies and the larger ordered moments determined independently by neutron diffraction strongly suggests that the dominant factor is the increase in the ordered Cr moment. We therefore regard the observed frequency evolution as a reliable indicator of the moment enhancement, while acknowledging that contributions from changes in the local muon environment cannot be fully excluded.

The analysis of the ambient pressure μ^+SR data for $NaCr_2O_4$ $[x = 1]$ is treated in greater detail elsewhere [37]. The muon signal was found to be well modeled by cosine functions with two well-defined frequencies: $\nu_{AF1} = 41.8(2)$ MHz and $\nu_{AF2} = 60.9(3)$ MHz:

$$\begin{aligned} A_0\, P_{ZF}(t) = {} & A_{AF1} \cos\left(2\pi\nu_{AF1}t + \frac{\pi\phi_{AF1}}{180}\right) \cdot e^{(-\lambda_{AF1}t)} \\ & + A_{AF2} \cos\left(2\pi\nu_{AF2}t + \frac{\pi\phi_{AF2}}{180}\right) \cdot e^{(-\lambda_{AF2}t)} \\ & + A_{tail} \cdot e^{(-\lambda_{tail}t)}. \end{aligned} \quad (2)$$

This is consistent with the development of distinct internal magnetic fields at two inequivalent muon stopping sites, both originating from the same commensurate canted AFM spin structure determined by neutron diffraction [37]. In that previous μ^+SR/NPD study, the temperature evolution of the asymmetries and the absence of any structural or magnetic transition demonstrated that ν_{AF1} and ν_{AF2} arise from

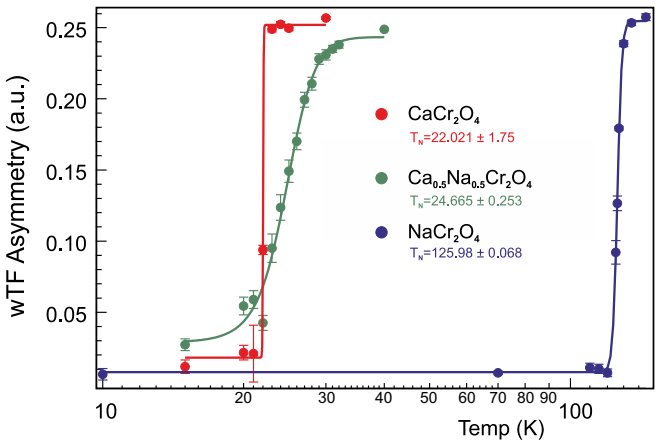

FIG. 4. Temperature dependencies of the transverse field asymmetries, extracted from the fit of the wTF μ^+SR spectra, for the three samples. The solid lines are fits to the sigmoid function, which provides their respective transition temperatures. The x axis is represented in logarithmic scale for clarity of display, given the broad range of the transition temperatures in these samples.

inequivalent μ^+ sites within a single long-range ordered phase, rather than from distinct magnetic phases.

2. *wTF-μ^+SR results*

In the wTF geometry an external magnetic field is applied orthogonal to the initial direction of the muons spin, causing it to precess in the plane perpendicular to the external field's direction. In this configuration, μ^+SR time spectra have been acquired for the three samples in the temperature ranges from 2 K to 30 K for $CaCr_2O_4$, from 2 K to 40 K for $Ca_{0.5}Na_{0.5}Cr_2O_4$, from 2 K to 145 K for $NaCr_2O_4$. For all the samples the applied transverse field has been set to wTF = 50 G, which is several orders of magnitude smaller than the internal field at the muon sites.

The fit function for the wTF spectra of the three samples is the following:

$$\begin{aligned} A_0\, P_{\mathrm{TF}}(t) = {} & A_{\mathrm{ZF(x)}} \cdot f_{(x)}(\nu, t, \phi) \\ & + A_{\mathrm{TF}} \cos\left(2\pi\, \nu_{\mathrm{TF}} t + \frac{\pi\phi}{180}\right) \cdot e^{(-\lambda_{\mathrm{TF}} t)} \\ & + A_{\mathrm{tail}} \cdot e^{(-\lambda_{\mathrm{tail}} t)}. \end{aligned} \tag{3}$$

Here A_0 is the initial asymmetry; $P_{TF}(t)$ is the muon spin polarization function; $A_{ZF(x)} \cdot f_{(x)}(\nu, t, \phi)$ represents the zero-field depolarization function specific to each sample, which also contributes to the early-time signal observed in the TF spectra; A_{TF} and A_{tail} are the asymmetries of the transverse field and tail polarization components; ν_{TF} is the frequency of the Larmor precession related to the applied wTF; ϕ is the initial phase of the oscillating signal; and λ_{TF} and λ_{tail} are the depolarization rates of the transverse field and tail components. The transition temperature for all the samples can be determined from the temperature dependence of the fitting parameter A_{TF} (plotted in Fig. 4). Here an increase of A_{TF} is observed as T increases, bringing the system from the magnetically ordered state to the paramagnetic state. The trend of the asymmetries has been fitted with a sigmoid function and the transition temperature is defined as the midpoint of the fitting curve.

A clear compositional dependence is observed for T_N, which increases dramatically as the sodium content increases, as also reported in a previous μ^+SR study carried out on the same system [65]. This shift follows the increase in the density of the ligand holes, which are the mediators of the double exchange interactions responsible for the magnetic ordering [37], as well as the shortening of the Cr-Cr distances. It is worth noticing that the transition temperatures for $CaCr_2O_4$ (22.15 K) and $Ca_{0.5}Na_{0.5}Cr_2O_4$ (24.70 K) are close, despite their clear compositional difference. This behavior suggests that T_N does not display strong sensitivity to the chemical variable at low Na content and that a threshold ligand-hole density must be exceeded before double exchange begins to dominate. As a result, more substantial changes in the transition temperature are only observed for Na concentrations above 80% [65].

There is, however, a clear difference in the trend of the three asymmetries: While $CaCr_2O_4$ and $NaCr_2O_4$ show a sharp transition, reaching the saturation abruptly, for $Ca_{0.5}Na_{0.5}Cr_2O_4$ the transition occurs with a lower rate and the full asymmetry is only recovered well above T_N. This phenomenon can be probably interpreted in terms of a broad "phase separation" since, in $Ca_{0.5}Na_{0.5}Cr_2O_4$, half of the Ca sites are occupied by Na ions. Therefore, the inhomogeneity in the sample composition, and the large gap between the transition temperatures of the two well-defined commensurate and incommensurate phases at the extremes of the solid solution, results in this gradual increase of the TF asymmetry as different parts of the sample achieve the paramagnetic state. Previous interpretations for the behavior of the muon depolarization in $Ca_{0.5}Na_{0.5}Cr_2O_4$ suggested the occurrence of a spin-glass state [65]. Given the aforementioned arguments, along with the occurrence of the long range IC order observed in the ZF spectra, this possibility should be probably disregarded (Fig. 3).

3. *μ^+SR results under applied pressure*

The chemical substitution not only intensifies the magnetic interactions but also alters the lattice volume, effectively acting as a microscopic "chemical pressure." However, substitution also changes other key parameters, such as the Cr valence state. Applying external hydrostatic pressure therefore provides a way to disentangle these effects in $Ca_{1-x}Na_xCr_2O_4$. Assuming that the chemical pressure is responsible for the changes in the magnetic structure of the solid solution, a reasonable expectation is that the application of an external hydrostatic compression should induce a shift in T_N towards higher values and possibly alter the magnetic exchange coupling mechanism in this material, hereby causing the emergence of novel magnetic phase transitions [27].

For each sample different pressures were applied (through the setup described in Sec. II): approximately. 0, 16, and 30 kbar for $CaCr_2O_4$; approximately. 0, 14, and 21 kbar for $NaCr_2O_4$; and approximately. 0, and 20 kbar for $Ca_{0.5}Na_{0.5}Cr_2O_4$. A ZF μ^+SR pressure-dependent experiment has been performed on the three samples at $T = 5$ K. Figure 5 shows a comparison between the muon spectra

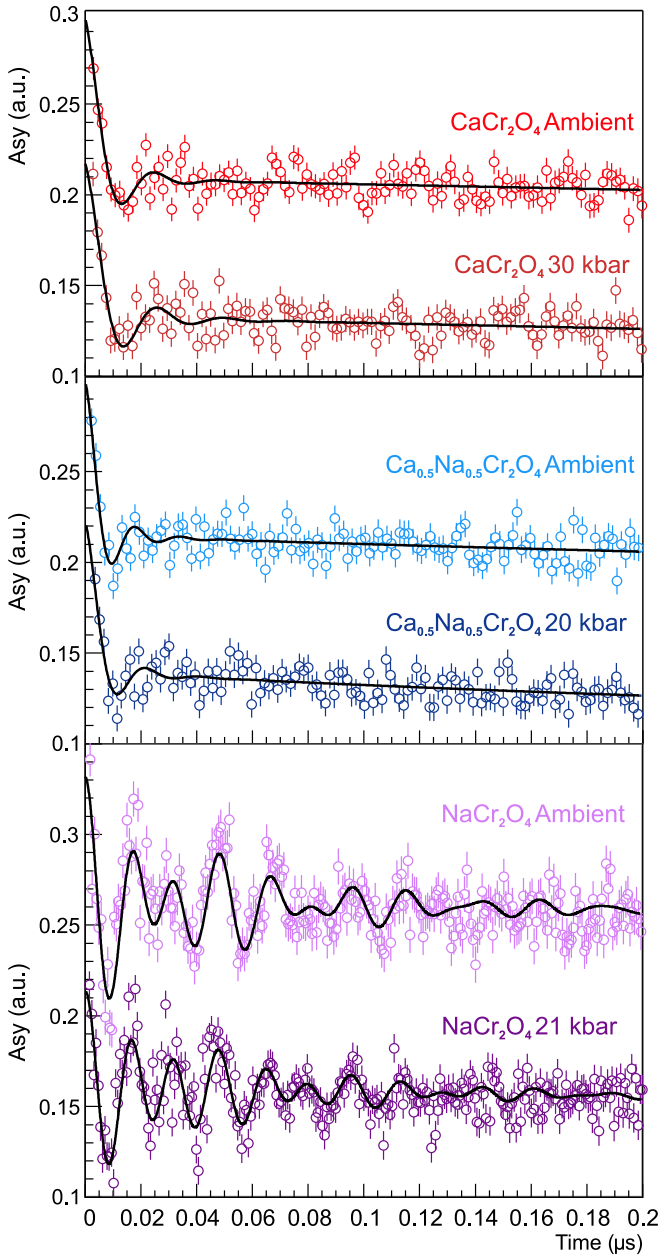

FIG. 5. Early-time-domain μ^+SR spectra in zero field at base temperature for $CaCr_2O_4$ (red data), $Ca_{0.5}Na_{0.5}Cr_2O_4$ (blue data), and $NaCr_2O_4$ (violet data) with the respective pressures. For clarity of display, these spectra are shifted along the y axis.

collected in ambient and maximum pressure applied at base temperature for the three samples. The fit functions for the spectra in high pressure are the same as the ones chosen for the ambient pressure data. This suggests that the application of a physical pressure does not induce novel magnetic phases in the solid solution, and the dramatic change observed in the spin structure as a function of the composition is mainly due to the changes in the ligand hole density.

Small differences between the muon polarization functions in ambient and high pressure can be found in the value of the muon precession frequencies for the Na doped samples. Here $Ca_{0.5}Na_{0.5}Cr_2O_4$ experiences a slight decrease in ν_{SDW} as the pressure increases, i.e., 62(6) MHz → 51(8) MHz. While such a decrease could suggest a reduction of the magnetic moment, the change lies within experimental uncertainty and therefore does not provide conclusive evidence of magnetic moment suppression in this pressure range.

In $NaCr_2O_4$, the two signals are both well fitted by cosine functions with two well-defined frequencies, whose respective values are equal within the error bars, i.e., $\nu_{AF1} = 42.8(3)$ MHz and $\nu_{AF2} = 61.4(3)$ MHz for the ambient pressure signal, $\nu_{AF1} = 43.1(5)$ MHz and $\nu_{AF2}62.5(2)$ MHz for the 21 kbar signal. We note that, due to the limited statistics of the base-temperature ZF-μ^+SR spectra, particularly in the first tens of nanoseconds, small differences between alternative depolarization functions (such as Bessel-type and dynamic Lorentzian Kubo-Toyabe forms) cannot be fully resolved in a completely model-independent way. Nevertheless, the use of a zeroth-order Bessel depolarization for $x = 0$ and $x = 0.5$ is motivated by the fact that it is a standard μSR response expected for an incommensurate spin-density-wave (or helimagnetic) state, reflecting the corresponding distribution of quasistatic internal fields at the muon site. This is consistent with the established incommensurate magnetic structure of the parent compound (from neutron diffraction) as well as with the overall quality and stability of the fits across the series.

While the frequencies themselves remain essentially unchanged with pressure, the ratio of their asymmetries (amplitudes) changes substantially. In particular, $A_{AF2}/A_{AF1} \sim 2$ in ambient pressure and $A_{AF2}/A_{AF1} \sim 3.6$ under 21 kbar. This suggests that pressure does not introduce a new internal-field scale or a distinct magnetic phase within our resolution. However, the change in relative amplitudes can reflect either a redistribution of site weighting or a pressure-dependent change in relaxation/visibility.

The evolution of the amplitude ratio is therefore attributed to changes in the relative spectral weights of the two oscillatory components (e.g., relative site populations and/or pressure-dependent relaxation/visibility), while the precession frequencies remain unchanged within uncertainties. In light of our previous μ^+SR/NPD study [37], where ν_{AF1} and ν_{AF2} were shown to arise from inequivalent muon environments within the same commensurate canted AFM phase, the pressure dependence of A_{AF2}/A_{AF1} can be interpreted as a redistribution of two coexisting internal-field components within a single long-range ordered state, rather than as a transition between distinct magnetic phases. Neutron diffraction shows a continuous reduction of the magnetic Bragg intensity with pressure, i.e., a progressive weakening of long-range magnetic order. In ZF-μ^+SR such weakening can manifest as a loss of oscillatory visibility of one component (enhanced damping/dynamics and/or a reduced ordered fraction associated with that component), producing a change in A_{AF2}/A_{AF1} even when the characteristic fields (frequencies) are unchanged. In this qualitative sense, the pressure-driven redistribution of μ^+SR spectral weight is consistent with the diffraction evidence for suppression of magnetic order; however, the present data do not allow a unique microscopic distinction between changes in muon-site weighting and changes in relaxation/visibility. Further high-resolution neutron diffraction under pressure would be

required to resolve possible subtle changes in canting and/or ordered volume fraction.

The presence of the nonmagnetic pressure cell introduces a higher background and an additional static component in the muon polarization function, which affects the long-time domain [27]. The trend of the asymmetry in the long-time domain is therefore well modeled by a static Gaussian Kubo-Toyabe function, which is commonly used to describe the muon spin polarization in randomly oriented nuclear dipolar fields. Indeed, all the ZF spectra in pressure cell have been fitted with the same functions described in Sec. III A with the addition of a static Kubo-Toyabe for a Gaussian field distribution of width Δ:

$$A_{\mathrm{KT}} G_{\mathrm{SGKT}}(\Delta, t), \tag{4}$$

whose explicit expression is as follows:

$$G_{\mathrm{SGKT}} = \tfrac{1}{3} + \tfrac{2}{3}[1 - (\sigma t)^2] e^{[-\frac{1}{2}(\sigma t)^2]}. \tag{5}$$

Here $\sigma[\mu s^{-1}]$ is given by $\sigma = \gamma_\mu \Delta$.

A wTF μ^+SR experiment has been performed on the three samples for different temperatures at each pressure. As discussed in Sec. III A, the wTF spectra have been fitted with an exponentially relaxing cosine function, the temperature evolution of the asymmetry has been extracted and fitted with a sigmoid function to obtain the transition temperatures for each sample at different pressures. The result of this analysis is shown in Fig. 6.

As clearly seen in Fig. 6, T_N shows very weak sensitivity to pressure-induced structural changes, in all the three samples. In particular, the transition temperature increases of about 1 K for $CaCr_2O_4$ and stays almost constant for $Ca_{0.5}Na_{0.5}Cr_2O_4$. Concerning $NaCr_2O_4$, T_N is linearly shifting towards lower values as the applied pressure increases. This behavior is consistent with an overall suppression of the magnetic order in $NaCr_2O_4$, suggesting that hydrostatic pressure primarily weakens the magnetic correlations between Cr ions. The temperature/pressure phase diagram of the solid solution $Ca_{1-x}Na_xCr_2O_4$ is displayed in Fig. 7.

Within the explored pressure range, all these effects are generally very weak, especially when compared to the effect of chemical substitution, where the transition temperature shifts by several tens of kelvin (but only for high Na concentrations). This suggests that more pronounced changes might only emerge under substantially higher applied pressures. At the same time, the fact that the ZF μ^+SR spectra could be fitted with the same functions at all pressures indicates that the magnetic phase itself remains robust within the studied regime. Taken together, these observations show that the ligand-hole density associated with Na substitution plays the dominant role in determining the exchange interactions and magnetic ground state in $Ca_{1-x}Na_xCr_2O_4$, whereas lattice compression provides only a secondary tuning effect.

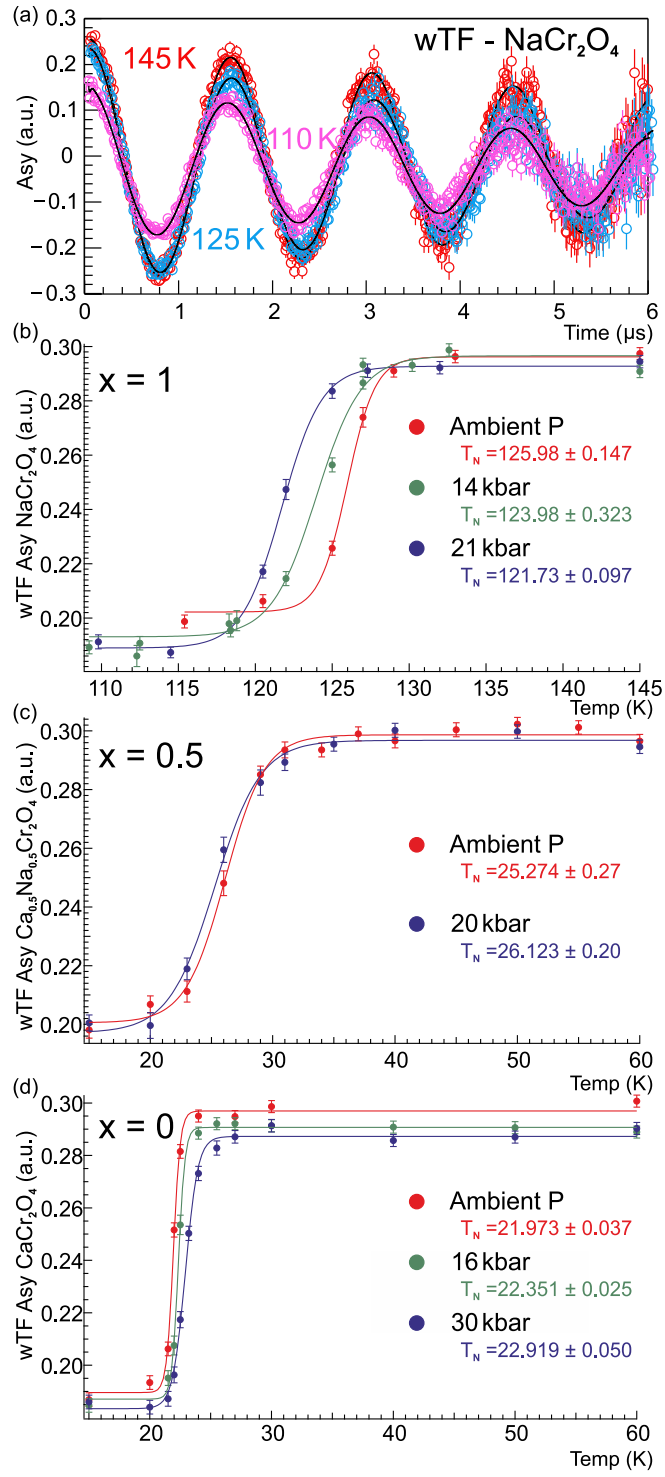

FIG. 6. (a) Weak transverse field μ^+SR spectra in the long-time domain at 110 K $< T <$ 145 K for $NaCr_2O_4$ under 21 kbar pressure. [(b), (c), and (d)] wTF μ^+SR asymmetries plotted as a function of temperature and pressure for the three samples, with their respective transition temperatures.

B. High-pressure neutron diffraction study

The magnetic transition of $NaCr_2O_4$ was investigated by pressure-dependent neutron powder diffraction. The transition temperature of $NaCr_2O_4$ is $T_N = 125.4$ K at ambient pressure and, according to the μ^+SR results, it was expected to decrease with higher applied pressures, until the full suppression of the magnetic ordering. In order to follow the magnetic transition as a function of pressure, the sample temperature was fixed at 100 K and diffraction patterns for each pressure point between ambient and 43 kbar were acquired in both

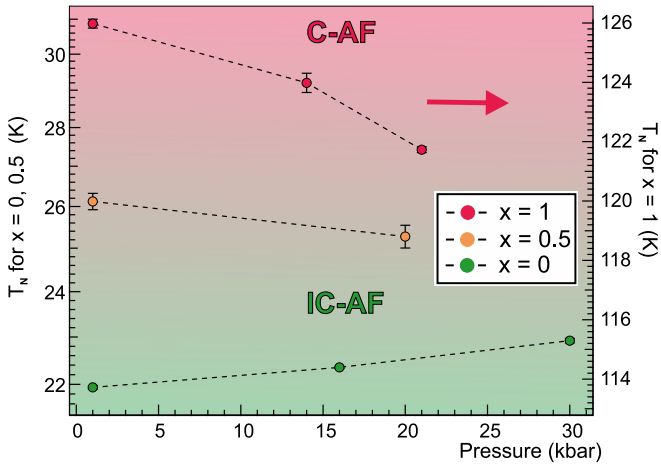

FIG. 7. Pressure dependence of the transition temperature for the three samples obtained from wTF μ^+SR data. The y axis representing the T_N of $NaCr_2O_4$ is on the right side of the plot for clarity of display.

the transverse and longitudinal configurations of the PEARL diffractometer, described in Sec. II B. The data acquired in transverse configuration were used to determine the exact value of the applied pressure by refining the lattice parameters of the lead calibrant. Figure 8 shows the diffraction patterns for $NaCr_2O_4$ in longitudinal configuration at room temperature and at 100 K in ambient pressure. The intensity of the scattered neutrons are displayed as a function of d spacing. Owing to the unusually large ordered Cr moment in $NaCr_2O_4$, estimated as 4.30(1) μB [37] and arising from ligand-hole–stabilized high-spin states in the negative charge-transfer regime, the magnetic [0 0 –1] reflection gives rise to a diffraction peak strong enough to be clearly visible in our accessible temperature range around $d \sim 9$ Å. In this framework, the ligand holes prevent static Cr^{3+}/Cr^{4+} charge ordering and stabilize effective d^4 ($S = 2$) configurations,

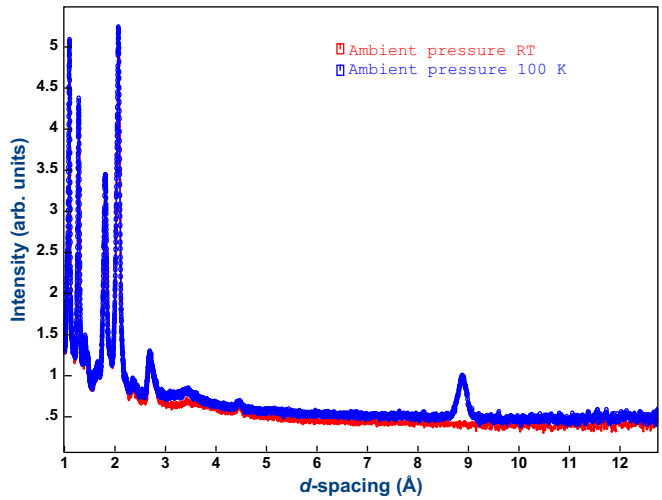

FIG. 8. PEARL ambient pressure diffraction patterns for $NaCr_2O_4$ in longitudinal configuration at room temperature (red curve) and 100 K (blue curve) in d spacing.

which naturally account for the enhanced ordered moment without invoking orbital contributions.

The evolution of the magnetic order as a function of pressure and temperature is tracked by following the evolution of the integrated intensity of the strong magnetic Bragg reflection [0 0 –1] displayed in Figs. 9(a) and 9(b). In Fig. 9(c) the temperature dependence of the integrated intensity of such magnetic peak under 43 kbar pressure, measured in PEARL-ISIS, is compared with the data on the same sample in ambient pressure measured in iMATERIA–J-PARC (from Ref. [37]) in the temperature range from 100 K to 130 K. The continuous line is a fit to the power law:

$$f(x) \propto \left(1 - \frac{x}{T_c}\right)^{\beta}. \tag{6}$$

While the onset of the magnetic transition temperature clearly shifted from iMATERIA's 130.00(3) K to PEARL's 120.6(2) K, a good fit for both the curves can be achieved by fixing the value of the critical exponent β to the value obtained for the iMATERIA data over the full temperature range (from 5 K to 130 K), $\beta \sim 0.25$, which is the fit shown in Fig. 9(c). When β is instead treated as a free parameter in the PEARL data, the fit yields $\beta = 0.283 \pm 0.057$, statistically compatible with the tricritical value of 0.25. The reduced χ^2 values of the curves with fixed and unfixed β are roughly of the same order of magnitude, confirming that the fit quality is essentially unchanged, and the resulting curves are indistinguishable by eye on the scale of Fig. 9(c). Given the limited statistics and sparse temperature coverage near T_N in the pressure data, this agreement should be regarded as consistency with tricritical behavior rather than a precise determination of the critical exponent. This behavior suggests that the antiferromagnetic-paramagnetic phase transition in $NaCr_2O_4$ is located at the tricritical point [37] regardless the pressure conditions, endorsing the hypothesis that the effect of pressure on $NaCr_2O_4$ is to merely suppress the magnetic order.

As established in Ref. [37], $NaCr_2O_4$ hosts a commensurate canted AFM component with propagation vector $\mathbf{k}_1 = (1\,0\,1)$ and a weaker long-period incommensurate component with $\mathbf{k}_2 \approx (0\,0\,\frac{1}{2})$. The strong magnetic reflection at $d \simeq 9$ Å, indexed as [0 0 –1], is dominated by the commensurate $\mathbf{k}_1$ component carrying the larger ordered moment, whereas the incommensurate component gives rise to much weaker satellites at larger d and diffuse magnetic scattering. Within the restricted Q range and background conditions of the high-pressure setup, these incommensurate satellites cannot be reliably tracked, so the pressure dependence of the [0 0 –1] intensity primarily reflects the evolution of the commensurate C-AFM order parameter.

Figure 9(d) displays the pressure dependence of the magnetic structure factor amplitude of the [0 0 –1] reflection F[0 0 –1] (which is proportional to the ordered moment). The latter decreases linearly as the pressure increases, consistent with the monotonic reduction of T_N with pressure revealed by our wTF-μ^+SR measurements on the same sample (Fig. 6), i.e., both probes indicate a progressive weakening of the long-range antiferromagnetic order in $NaCr_2O_4$. From the linear fit to the data it is possible to extrapolate the critical

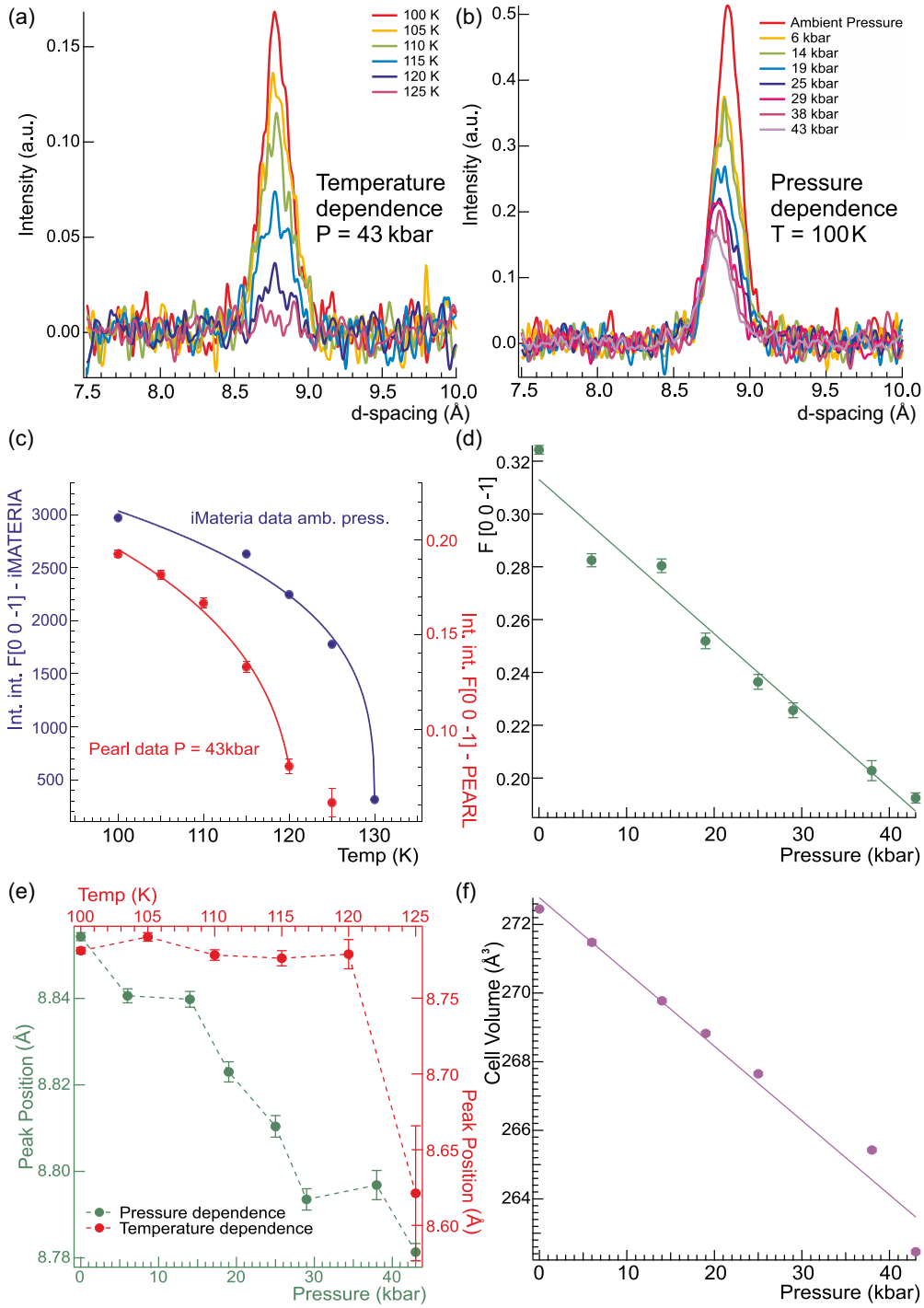

FIG. 9. (a) Intensity of the magnetic peak corresponding to the [0 0 –1] reflection versus d spacing under 43 kbar pressure as function of temperature. (b) Intensity of the magnetic peak corresponding to the [0 0 –1] reflection versus d spacing at 100 K temperature as function of pressure. (c) Structure factor of the magnetic peak corresponding to the [0 0 –1] reflection from PEARL at 43 kbar pressure (red data) and iMATERIA in ambient pressure (blue data). For clarity of display, the y axis for the iMATERIA data is displayed on left side of the plot while the PEARL data on the right. The continuous line is a fit to the power law in Eq. (6). (d) Square root of the integrated intensity of the magnetic peak corresponding to the [0 0 –1] reflection as a function of pressure. The continuous line is a linear fit. (e) Pressure dependence (bottom left, green plot) and temperature dependence (top right, red plot) of the magnetic peak position in d spacing. (f) Pressure dependence of the cell volume in $NaCr_2O_4$.

pressure which would completely suppress the magnetic order in $NaCr_2O_4$: $P_c = 107(8)$ kbar. Figure 9(e) shows the temperature and pressure dependence of the magnetic peak position, obtained by fitting the magnetic peak to a Gaussian function. No significant difference is observed as the temperature changes while a major shift towards lower d values occurs as the pressure increases, due to the reduction in unit-cell volume [Fig. 9(f)]. The fact that the magnetic peak in

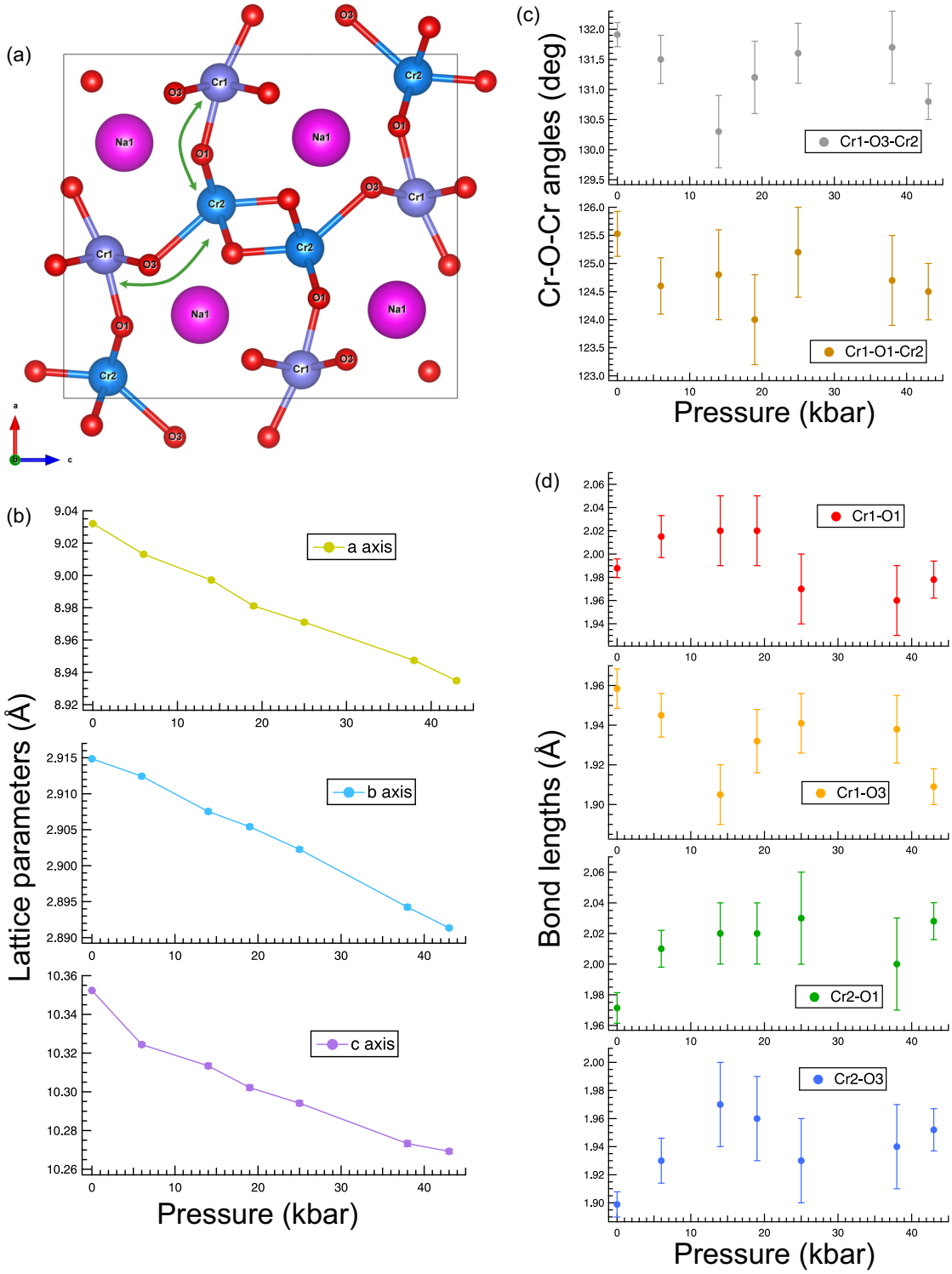

FIG. 10. (a) Schematic of $NaCr_2O_4$ crystal structure with the Cr1/Cr2 and O1/O3 sites explicitly labeled and the Cr–O–Cr bonds of interest highlighted by green arrows. (b) Pressure-dependent trends of the lattice parameters *a*, *b* and *c*, the straight line is a guide to the eye. (c) Pressure-dependent trends of the Cr1-O3-Cr2 and Cr1-O1-Cr2 angles. (d) Pressure-dependent trends of the short Cr–O bond lengths.

$d \sim 9$ Å does not undergo any major change (e.g., splitting) as a function of pressure, is consistent with the absence of alterations in the magnetic ground state of $NaCr_2O_4$.

To quantify possible pressure-driven changes of the Cr–O network, we extracted Cr–O distances and Cr–$\widehat{O}$–Cr angles from Rietveld-refined *Pnma* models (transverse bank, 100 K) and propagated the crystallographic uncertainties from the refinement's covariance [Fig. 10(a)]. This choice of bonds/angles targets the two corner-sharing bridges Cr_1–O_1–Cr_2 and Cr_1–O_3–Cr_2, which (i) host the ligand holes

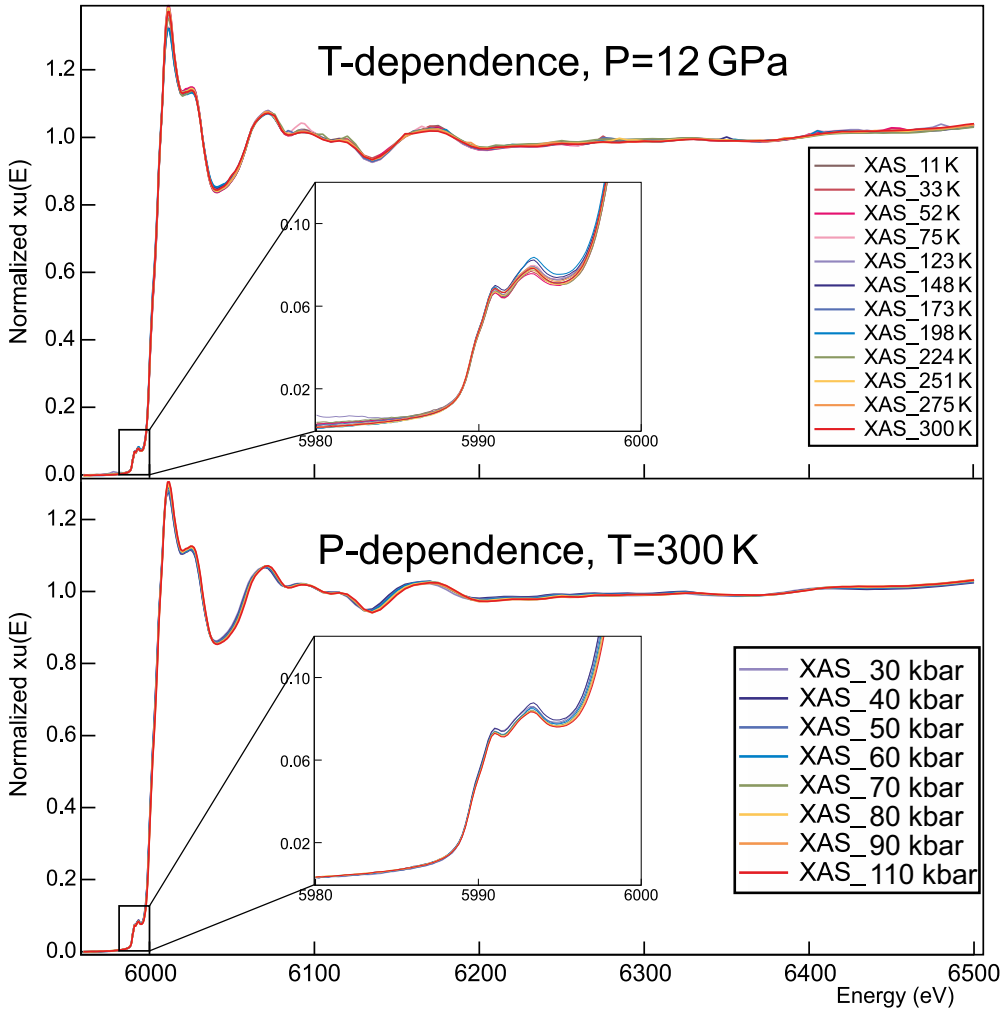

FIG. 11. Pressure- and temperature-dependent XAS spectra for $NaCr_2O_4$. The insets show a magnification of the pre-edge in the absorption near edge structure.

and (ii) set the dominant interchain exchange in $NaCr_2O_4$; by contrast, the edge-sharing O_2/O_4 connections along the *b* axis contribute little to the exchange balance [37]. The unit-cell volume contracts linearly by $\sim$% on increasing the applied load up to 43 kbar. The contraction is essentially isotropic, as seen from the pressure trends of the individual lattice parameters, all of them showing reductions of $\sim$1% [Fig. 10(b)].

Despite these clear trends, the key superexchange angles Cr_1–$\widehat{O}_1$–Cr_2 and Cr_1–$\widehat{O}3$–Cr_2 show no resolvable evolution within uncertainties and the four short bonds Cr1-O1, Cr2-O1, Cr1-O3, Cr2-O3 are likewise pressure insensitive within the error [Figs. 10(c) and 10(d)]. This apparent discrepancy is explained by the framework's "rigid-unit" response: most of the compressibility is accommodated by small octahedral tilts and by contraction of the channel hosting the alkali-ion sublattice, while the corner-sharing Cr–O–Cr geometry that governs superexchange remains geometrically constrained and thus nearly invariant. Any residual changes in Cr–O–Cr angles and Cr-O bond distances are below our detection limits ($\lesssim$0.4° and $\lesssim$0.02 Å over the full range). Thus, within the precision afforded by these PEARL transverse-bank data (used primarily for *in situ* load calibration via Pb), the local Cr–O–Cr geometry governing superexchange is essentially unchanged under compression.

C. XAS results under applied pressure

The evolution of the local electronic structure for the full family $Ca_{1-x}Na_xCr_2O_4$ has been previously studied as a function of the Na content by XAS in ambient pressure (L edge for Cr and K edge for O) [38]. Here remarkable changes in the Cr valence state were observed, due to the partial oxidation of Cr^{3+} to Cr^{4+} between $CaCr_2O_4$ and the Na-doped $CaCr_2O_4$.

Our XAS experiment was intended to be an initial step in the study of the electronic structure of $NaCr_2O_4$ by tuning exchange via compression/bandwidth in the CrO_6 chains, through the application of an external pressure. For this purpose, we performed a systematic pressure-dependent XAS study on stoichiometric $NaCr_2O_4$ in the pressure range [0–124] kbar, temperature range [10–300] K and EXAS energy range [5.9–6.5] keV, and therefore we acquired Cr 1s XAS spectra in the Cr metal-K edge.

Figure 11 displays our normalized XAS spectra (pre-edge in the inset), measured at a fixed pressure of 124 kbar for different temperature points (top panel), and measured at a fixed

temperature of 300 K for different pressure points (bottom panel).

No change is visible for both the near-edge and extended x-ray absorption structures, in the low- and high-kinetic-energy range for the detected photoelectrons, as a function of pressure and temperature. This indicates that compression does not change the average Cr valence state or the gross local coordination within the sensitivity of Cr K-edge XAS. At the same time, μ^+SR and neutron diffraction show that long-range order in $NaCr_2O_4$ is progressively weakened under pressure (decreasing T_N and magnetic Bragg intensity) while no new magnetic symmetry emerges. We therefore conclude that the pressure effect is not associated with a resolvable change of the average Cr oxidation state but rather with subtler electronic renormalizations (e.g., bandwidth/hybridization) that are not captured at the present K-edge resolution. Additional XAS pressure-dependent experiments focused on the Cr L_2 and L_3 edges and on the O K edge would be relevant to test whether pressure modifies the balance between DE and the AFM correlated-hopping channel in $NaCr_2O_4$ (e.g., via bandwidth enhancement and/or subtle changes in ligand-hole character), ultimately suppressing long-range C-AFM order at $P_c = 107(8)$ kbar.

D. Discussion

Notably, even though the Cr K-edge XAS and the Rietveld refinements show no resolvable changes in the local Cr electronic structure or in the corner-sharing Cr–O–Cr geometry over our pressure range, the magnetic structure factor amplitude F[0 0 –1] decreases linearly with pressure and μ^+SR indicates a redistribution between muon sites/changes in relaxation/visibility. These apparent inconsistencies can be reconciled within the ligand-hole/negative charge-transfer picture established previously [35,37,41,42]. $NaCr_2O_4$ is mixed-valent and negative charge-transfer, hosting ligand holes on O (O 2*p*) that mediate double exchange (DE) on the corner-sharing Cr–O–Cr bridges. Its magnetism results from a competition: ferromagnetic DE on Cr1-O3-Cr2 and an AFM correlated-hopping (superexchange-like) channel on Cr1-O1-Cr2. Specifically, in the commensurate C-AFM spin structure determined previously [37], the Cr1–O3–Cr2 bonds within the rutile slabs (approximately along the *c* axis) support predominantly ferromagnetic double exchange, aligning spins ferromagnetically along *c*, while the orthogonal Cr1–O1–Cr2 bonds (running mainly along *a*) couple these ferromagnetic chains antiferromagnetically. In this sense, the magnetic ground state arises from coexisting ferromagnetic exchange on the Cr1–O3–Cr2 bonds and antiferromagnetic exchange on the Cr1–O1–Cr2 bonds within the same Cr network.

Motivated by this bandwidth/hybridization tuning, it is useful to recall that the dominant exchange scales in negative charge-transfer oxides depend primarily on the Cr–O covalency, encoded in the *p-d* hopping t_{pd}, and on the ligand-hole density, rather than on small geometry changes. Following the classic treatments of double exchange and superexchange, one may write schematic scaling relations as:

$$J_{\mathrm{DE}} \propto t_{pd}\, n_{\mathrm{hole}}, \quad J_{\mathrm{AF}} \propto \frac{t_{pd}^2}{U + \Delta_{\mathrm{eff}}}. \tag{7}$$

Here n_{hole} denotes the density of ligand holes, U the on-site Coulomb repulsion, and Δ_{eff} the effective charge-transfer energy. Increasing the Cr–O hybridization t_{pd}, therefore, boosts both types of exchange, linearly for the FM double exchange (reflecting the kinetic energy gain) and quadratically for the AFM superexchange (as a second-order virtual hopping process). In this schematic picture, the AFM superexchange scale depends explicitly on the correlation and charge-transfer energies ($U + \Delta_{\mathrm{eff}}$) and can therefore respond differently to pressure-induced changes in covalency and screening than the kinetic (DE-like) scale. Empirically, the Na–Ca doping study and spectroscopic data support these dependencies: Reducing the hole count or Cr–O covalency (for instance, by Ca substitution) weakens the FM exchange and eventually favors localized AF interactions [35]. Conversely, a highly covalent state with readily formed ligand holes (small Δ_{eff}) is a prerequisite for the robust 125 K magnetic order and the unusual coexistence of ferromagnetism and antiferromagnetism in $NaCr_2O_4$.

Within the ligand-hole framework, hydrostatic pressure primarily acts as an "electronic" tuning parameter: By reducing interatomic distances it increases the Cr–O overlap and therefore the effective *p-d* hopping amplitude t_{pd}, i.e., the kinetic-energy scale (bandwidth) of the itinerant Cr–O states. Such a renormalization can occur without any detectable change of the average Cr valence or gross local coordination at the Cr K edge, and without a resolvable evolution of the Cr-O-Cr geometry within the present diffraction resolution. In $NaCr_2O_4$, long-range order is established by locking together exchange interactions that are realized on distinct corner-sharing bridges (O_3- and O_1-mediated links) and therefore depends not only on the overall magnitude of exchange, but on the relative balance and anisotropy between these channels. A modest pressure-induced increase of t_{pd} can reweight the contributions of these competing exchange channels and enhance fluctuations/frustration of the canted-AFM state, thereby reducing the temperature at which coherent long-range order sets in. This provides a natural microscopic context for the observed suppression of T_N in μ^+SR and the monotonic reduction of the [0 0 –1] magnetic Bragg intensity with pressure, despite the absence of resolvable structural distortions.

A convenient way to frame this competition is in terms of the bandwidth W of the itinerant states. In a simplified picture, W is set by the product of the hopping strength and the number of connected neighbors (coordination z), e.g., $W \sim 2zt_{pd}$ for a half-filled band [66]. Because the low-energy electronic states in $NaCr_2O_4$ have substantial hybridized Cr 3*d*–O 2*p* character, changes in t_{pd} naturally translate into changes in the itinerancy (bandwidth) of the ligand-hole network. Hydrostatic pressure, by increasing orbital overlap, enhances t_{pd} and thus W. In this qualitative sense, increasing itinerancy can destabilize the commensurate ordered state (via reweighting of exchange channels and enhanced fluctuations), lowering T_N even if the underlying exchange scales increase under pressure, consistent with the observed suppression of T_N and magnetic Bragg intensity.

The sensitivity of $NaCr_2O_4$ to such subtle electronic tuning is consistent with its magnetic transition being located near a tricritical point. At such a boundary, where FM and AFM channels are finely balanced, even a few-percentages increase

in t_{pd} (and thus W), too small to be resolved at the XAS K edge, can disproportionately weaken AFM order. This explains why T_N and the magnetic Bragg intensity decrease with pressure despite the Cr–O–Cr geometry remaining unchanged within our structural resolution. Here it is worth to briefly comment on the possible role of the long-period incommensurate component reported in Ref. [37]. Our present μ^+SR data under pressure display a single magnetic transition and no unambiguous additional precession frequency or distinct relaxation channel that could be clearly assigned to a separate incommensurate phase, while the neutron measurements under pressure are restricted to the main [0 0 –1] reflection of the commensurate $\mathbf{k}_1$ structure. We therefore interpret the observed suppression of T_N and of the [0 0 –1] intensity primarily in terms of changes within the commensurate C-AFM component. Nevertheless, a pressure-induced redistribution of spectral weight between the commensurate and incommensurate components is an appealing scenario. Such a change could reduce the [0 0 –1] intensity and subtly modify the local field distribution at the muon sites. Our current dataset does not allow us to resolve this possibility, high-resolution neutron diffraction measurements under pressure that can follow both propagation vectors will be required to address it quantitatively.

It is also relevant that $NaCr_2O_4$ itself is synthesized only under very high pressures ($\sim$7 GPa). This implies that the ambient-pressure compound is already in a metastable, highly covalent state optimized for strong Cr–O overlap and mixed valence. Additional pressure therefore acts mainly as a bandwidth-tuning parameter rather than as a driver of structural reorganization. In this sense, our interpretation that the pressure effect is electronic rather than structural is well justified. A similar situation is seen in other mixed-valence Cr oxides, e.g., $K_2Cr_8O_{16}$, which undergoes a pressure-induced bandwidth-driven magnetic transition from a ferromagnetic metal to an antiferromagnetic insulator [27,67].

Finally, this perspective also clarifies why $CaCr_2O_4$ and $Ca_{0.5}Na_{0.5}Cr_2O_4$ are essentially insensitive to applied pressure in our μ^+SR data. Pure $CaCr_2O_4$ hosts no ligand holes, so its magnetism is governed by localized superexchange pathways that are robust against modest structural compression. The half-doped compound has a reduced hole density compared to $NaCr_2O_4$, placing it in a more localized regime where bandwidth tuning has little influence on the exchange balance. Only in the Na-rich end member, where DE and AFM interactions are finely poised, pressure induced bandwidth enhancement noticeably destabilizes long-range order.

IV. CONCLUSIONS

The members of the solid solution $Ca_{1-x}Na_xCr_2O_4$ with [$x = 0$, 0.5, 1] have been investigated under high pressure using μ^+SR, neutron diffraction and x-ray absorption spectroscopy. Our study shows that the application of hydrostatic pressure, aimed at tuning the magnetic exchange interactions among Cr ions while keeping the ligand hole density fixed in the CrO_6 chains, has only a limited influence on the magnetic ground state. Within the pressure range explored, the magnetic transition temperature in $CaCr_2O_4$ and $Ca_{0.5}Na_{0.5}Cr_2O_4$ is essentially pressure-independent whereas in $NaCr_2O_4$ it decreases slightly, consistent with a gradual weakening of the magnetic coupling mechanism and extrapolating to a complete suppression at a critical pressure of $P_c = 107(8)$ kbar.

If structural compression were the primary driver of the magnetic transformations observed in the Na-rich compound, then one would expect $CaCr_2O_4$ under pressure to evolve toward the $NaCr_2O_4$ state or at least to display a similar pressure trend. Instead, the two systems evolve differently, demonstrating that lattice compression alone cannot account for the observed changes. Thus, while ligand-hole density fixed by Na/Ca substitution is the dominant factor setting the magnetic ground state, hydrostatic pressure in $NaCr_2O_4$ provides a secondary tuning knob that weakens long-range AFM order through bandwidth enhancement. The absence of a comparable effect in $CaCr_2O_4$ confirms that ligand-hole physics, rather than structural compression, controls the phase diagram in $Ca_{1-x}Na_xCr_2O_4$. This finding highlights the broader importance of negative charge-transfer physics in high-valence transition-metal oxides. Electronic self-doping via ligand holes, rather than structural compression, dictates the balance of exchange interactions and stabilizes unusual high-spin configurations. In a wider context, this behavior resonates with recent discoveries in nickelate superconductors [68], where negative charge-transfer states also play a decisive role in shaping emergent electronic phases [69]. Our results thus position the chromates as a complementary platform to explore how ligand-hole physics governs magnetism and electronic correlations under external tuning parameters.

Future studies on intermediate compositions (e.g., $x =$ 0.1–0.2) and higher statistics at low temperature, especially under pressure, would be very valuable to further refine the distinction between different possible local-field distributions and to build on the ground work established here.

ACKNOWLEDGMENTS

The μ^+SR measurements were carried out at the instruments GPD and Dolly of the Swiss Muon Source (SμS) at PSI. The ND measurements were carried out at the instrument PEARL of the neutron spallation source ISIS. The XAS measurements were carried out at the instrument BL39XU of the synchrotron facility SPring-8. The authors thank J.-C. Orain, N. Matsubara, and H. Nozaki along with the staff of PSI, ISIS, and SPring-8 for the valuable help in the experimental measurements. This research is funded by the Swedish Foundation for Strategic Research (SSF) within the Swedish national graduate school in neutron scattering (SwedNess), as well as the SSF-Swedness Grant No. SNP21-0004 and the Foundation Blanceflor 2024 fellow scholarship, the Swedish Research Council VR (Grants No. Dnr. 2021-06157 and No. Dnr. 2022-03936), and the Carl Tryggers Foundation for Scientific Research (Grant No. CTS-22:2374). J.S. is supported by the Japan Society for the Promotion Science (JSPS) KAKENHI Grants No. JP18H01863, No. JP20K21149, and No. JP23H01840. H.S. acknowledged support by KAKENHI Grant No. JP25K00959. O.K.F is supported by the Swedish Research Council (VR) through Grant No. 2022-06217, the Foundation Blanceflor fellow scholarships for 2023 and 2024, and the Ruth and Nils-Erik Stenbäck Foundation. Y.S.

acknowledged funding from the Swedish Research Council (VR) through a Starting Grant No. (Dnr. 2017-05078) and the Knut and Alice Wallenberg Foundation through the Grant No. 2021.0150.

DATA AVAILABILITY

The data that support the findings of this article are openly available [70].

[1] R. E. Peierls, *Quantum Theory of Solids* (Oxford, Clarendon, 1964).

[2] M. Grioni, S. Pons, E. Frantzeskakis, Recent ARPES experiments on quasi-1D bulk materials and artificial structures, J. Phys.: Condens. Matter **21**, 023201 (2009).

[3] M. Nakamura, A. Sekiyama, H. Namatame, A. Fujimori, H. Yoshihara, T. Ohtani, A. Misu, M. Takano, Metal-semiconductor transition and Luttinger-liquid behavior in quasi-one-dimensional $BaVS_3$ studied by photoemission spectroscopy, Phys. Rev. B **49**, 16191 (1994).

[4] B. Lake, D. A. Tennant, C. D. Frost, S. E. Nagler, Quantum criticality and universal scaling of a quantum antiferromagnet, Nat. Mater. **4**, 329 (2005).

[5] A. Yoshimori, A new type of antiferromagnetic structure in the rutile type crystal, J. Phys. Soc. Jpn. **14**, 807 (1959).

[6] T. Masuda, A. Zheludev, H. Manaka, L.-P. Regnault, J.-H. Chung, and Y. Qiu, Dynamics of composite haldane spin chains in IPA-$CuCl_3$, Phys. Rev. Lett. **96**, 047210 (2006).

[7] L. Mihály, B. Dóra, A. Ványolos, H. Berger, and L. Forró, Spin-lattice interaction in the quasi-one-dimensional helimagnet $LiCu_2O_2$, Phys. Rev. Lett. **97**, 067206 (2006).

[8] A. C. Komarek, M. Isobe, J. Hemberger, D. Meier, T. Lorenz, D. Trots, A. Cervellino, M. Fernández-Díaz, Y. Ueda, and M. T. Braden, Dimerization and charge order in hollandite $K_2V_8O_{16}$, Phys. Rev. Lett. **107**, 027201 (2011).

[9] H. Nozaki, J. Sugiyama, M. Månsson, M. Harada, V. Pomjakushin, V. Sikolenko, A. Cervellino, B. Roessli, and H. Sakurai, Incommensurate spin-density-wave order in quasi-one-dimensional metallic antiferromagnet NaV_2O_4, Phys. Rev. B **81**, 100410(R) (2010).

[10] F. Damay, C. Martin, V. Hardy, A. Maignan, G. André, K. Knight, S. R. Giblin, and L. C. Chapon, Zigzag ladders with staggered magnetic chirality in the $S = \frac{3}{2}$ compound β-$CaCr_2O_4$, Phys. Rev. B **81**, 214405 (2010).

[11] H. Kawamura, Universality of phase transitions of frustrated antiferromagnets, J. Phys.: Condens. Matter **10**, 4707 (1998).

[12] N. Matsubara, E. Nocerino, K. Kamazawa, O. K. Forslund, Y. Sassa, L. Keller, V. V. Sikolenko, V. Pomjakushin, H. Sakurai, J. Sugiyama, and M. Mansson, Neutron powder diffraction study of $NaMn_2O_4$ and $Li_{0.92}Mn_2O_4$: Insights on spin-charge-orbital ordering, Phys. Rev. Res. **2**, 043143 (2020).

[13] Y. Ye, L. Dai, T. Sun, L. You, R. Zhu, J. Gao, R. Peng, D. Yu, and G. Qin, High-quality CdTe nanowires: Synthesis, characterization, and application in photoresponse devices, J. Appl. Phys. **108**, 044301 (2010).

[14] C. Cavallo, F. Di Pascasio, A. Latini, M. Bonomo, and D. Dini, Nanostructured semiconductor materials for dye-sensitized solar cells, J. Nanomater. **2017**, 31 (2017).

[15] T. Edvinsson, Optical quantum confinement and photocatalytic properties in two-, one- and zero-dimensional nanostructures, R. Soc. Open Sci. **5**, 180387 (2018).

[16] N. Sharma, J. Plevert, G. Subba Rao, B. Chowdari, and T. White, Tin oxides with hollandite structure as anodes for lithium ion batteries, Chem. Mater. **17**, 4700 (2005).

[17] X. Liu, X. Wang, A. Iyo, H. Yu, H. Zhou, *et al.*, High stable post-spinel $NaMn_2O_4$ cathode of sodium ion battery, J. Mater. Chem. A **2**, 14822 (2014).

[18] M. Månsson, I. Umegaki, H. Nozaki, Y. Higuchi, I. Kawasaki, I. Watanabe, H. Sakurai, and J. Sugiyama, Na-ion dynamics in quasi-1D compound NaV_2O_4, J. Phys.: Conf. Ser. **551**, 012035 (2014).

[19] C. Ling and F. Mizuno, Phase stability of post-spinel compound AMn_2O_4 (A= Li, Na, or Mg) and its application as a rechargeable battery cathode, Chem. Mater. **25**, 3062 (2013).

[20] L. A. Ma, R. Palm, E. Nocerino, O. K. Forslund, N. Matsubara, S. Cottrell, K. Yokoyama, A. Koda, J. Sugiyama, Y. Sassa, M. Månsson, *et al.*, Na-ion mobility in P2-type $Na_{0.5}Mg_xNi_{0.17-x}Mn_{0.83}O_2$ ($0 \leqslant X \leqslant 0.07$) from electrochemical and muon spin relaxation studies, Phys. Chem. Chem. Phys. **23**, 24478 (2021).

[21] E. Nocerino, O. K. Forslund, H. Sakurai, N. Matsubara, A. Zubayer, F. Mazza, S. Cottrell, A. Koda, I. Watanabe, A. Hoshikawa, *et al.*, Na-ion dynamics in the solid solution $Na_xCa_{1-x}Cr_2O_4$ studied by muon spin rotation and neutron diffraction, Sust. Energy Fuels **8**, 1424 (2024).

[22] K. Papadopoulos, O. K. Forslund, E. Nocerino, F. O. L. Johansson, G. Simutis, N. Matsubara, G. Morris, B. Hitti, D. Arseneau, P. Svedlindh, M. Medarde, D. Andreica, J. C. Orain, V. Pomjakushin, L. Borjesson, J. Sugiyama, M. Mansson, and Y. Sassa, Influence of the magnetic sublattices in the double perovskite $LaCaNiReO_6$, Phys. Rev. B **106**, 214410 (2022).

[23] E. Nocerino, C. Witteveen, S. Kobayashi, O. K. Forslund, N. Matsubara, A. Zubayer, F. Mazza, S. Kawaguchi, A. Hoshikawa, I. Umegaki, *et al.*, Nuclear and magnetic spin structure of the antiferromagnetic triangular lattice compound $LiCrTe_2$ investigated by μ^+ SR, neutron and x-ray diffraction, Sci. Rep. **12**, 21657 (2022).

[24] E. Nocerino, S. Kobayashi, C. Witteveen, O. K. Forslund, N. Matsubara, C. Tang, T. Matsukawa, A. Hoshikawa, A. Koda, K. Yoshimura, *et al.*, Competition between magnetic interactions and structural instabilities leading to itinerant frustration in the triangular lattice antiferromagnet $LiCrSe_2$, Commun. Mater. **4**, 81 (2023).

[25] E. Nocerino, J. Sugiyama, O. K. Forslund, I. Umegaki, S. Kobayashi, K. Yoshimura, Y. Sassa, and M. Månsson, Cr-Cr distance and magnetism in the phase diagram of triangular lattice antiferromagnets: A systematic comparative study, Phys. Rev. Mater. **8**, 084403 (2024).

[26] N. Matsubara, T. Masese, E. Suard, O. K. Forslund, E. Nocerino, R. Palm, Z. Guguchia, D. Andreica, A. Hardut, M. Ishikado, *et al.*, Cation distributions and magnetic properties of ferrispinel $MgFeMnO_4$, Inorg. Chem. **59**, 17970 (2020).

[27] O. K. Forslund, D. Andreica, Y. Sassa, H. Nozaki, I. Umegaki, E. Nocerino, V. Jonsson, O. Tjernberg, Z. Guguchia, Z. Shermadini, *et al.*, Magnetic phase diagram of $K_2Cr_8O_{16}$ clarified by high-pressure muon spin spectroscopy, Sci. Rep. **9**, 1141 (2019).

[28] J. Sugiyama, D. Andreica, O. K. Forslund, E. Nocerino, N. Matsubara, Y. Sassa, Z. Guguchia, R. Khasanov, F. L. Pratt, H. Nakamura, *et al.*, Magnetic phase boundary of $BaVS_3$ clarified with high-pressure μ^+ SR, Phys. Rev. B **101**, 174403 (2020).

[29] S. Klokishner, J. Linares, and F. Varret, Effect of hydrostatic pressure on phase transitions in spin-crossover 1D systems, Chem. Phys. **255**, 317 (2000).

[30] H. Karunadasa, Q. Huang, B. G. Ueland, J. W. Lynn, P. Schiffer, K. A. Regan, and R. J. Cava, Honeycombs of triangles and magnetic frustration in SrL_2O_4 (L G = Dd, Hy, Eo, Tr, Ym, and Yb), Phys. Rev. B **71**, 144414 (2005).

[31] A. Niazi, S. L. Bud'ko, D. L. Schlagel, J. Q. Yan, T. A. Lograsso, A. Kreyssig, S. Das, S. Nandi, A. I. Goldman, A. Honecker, R. W. McCallum, M. Reehuis, O. Pieper, B. Lake, and D. C. Johnston, Single-crystal growth, crystallography, magnetic susceptibility, heat capacity, and thermal expansion of the antiferromagnetic $S = 1$ chain compound CaV_2O_4, Phys. Rev. B **79**, 104432 (2009).

[32] D. Khomskii, Classifying multiferroics: Mechanisms and effects, Physics **2**, 20 (2009).

[33] H. Kikuchi, M. Chiba, and T. Kubo, Possible gapless chiral phase in a frustrated $S = 1$ 1D anti-ferromagnet, CaV_2O_4, Can. J. Phys. **79**, 1551 (2001).

[34] E. Nocerino, Emergent properties and the multiscale characterization challenge in condensed matter, from crystals to complex materials: A review, J. Phys. D **58**, 393001 (2025).

[35] H. Sakurai, Magnetic and electronic properties of $Ca_{(}1\text{-}x)NaXCr_2O_4$ double-exchange interactions and ligand holes, Phys. Rev. B **89**, 024416 (2014).

[36] O. Muller, R. Roy, *The Major Ternary Structural Families* (Springer Verlag, Berlin, 1974).

[37] E. Nocerino, O. K. Forslund, H. Sakurai, A. Hoshikawa, N. Matsubara, D. Andreica, A. Zubayer, F. Mazza, T. Saito, J. Sugiyama, *et al.*, Unusually large magnetic moment and tricritical behavior of the cmr compound $NaCr_2O_4$ revealed with high resolution neutron diffraction and Sr, J. Phys.: Mater. **6**, 035009 (2023).

[38] M. Taguchi, H. Yamaoka, Y. Yamamoto, H. Sakurai, N. Tsujii, M. Sawada, H. Daimon, K. Shimada, and J. Mizuki, Unusual coexistence of negative and positive charge transfer in mixed-valence $Na_xCa_{1\text{-}x}Cr_2O_4$, Phys. Rev. B **96**, 245113 (2017).

[39] H. Sakurai, T. Kolodiazhnyi, Y. Michiue, E. Takayama-Muromachi, Y. Tanabe, and H. Kikuchi, Unconventional colossal magnetoresistance in sodium chromium oxide with a mixed-valence state, Angew. Chem. Int. Ed. **51**, 6653 (2012).

[40] T. Toriyama, T. Konishi, and Y. Ohta, Electronic structure of calcium-ferrite-type Cr oxide $NaCr_2O_4$, in *Proceedings of the International Conference on Strongly Correlated Electron Systems (SCES2013)* (The Physical Society of Japan, Tokyo, Japan, 2014), p. 017003.

[41] H. Takeda, Y. Shimizu, M. Itoh, H. Sakurai, and E. Takayama-Muromachi, Magnetic frustration effects in the new colossal magnetoresistance oxide $NaCr_2O_4$, J. Kor. Phys. Soc. **62**, 1914 (2013).

[42] H. Yamaoka, E. F. Schwier, Y. Yamamoto, M. Nakatake, M. Sawada, H. Sakurai, N. Tsujii, M. Arita, H. Iwasawa, M. Taguchi, *et al.*, Electronic and crystal structures of $(Na_{1-x}Ca_x)Cr_2O_4$ with anomalous colossal magnetoresistance, Phys. Rev. B **102**, 235150 (2020).

[43] K. Momma and F. Izumi, VESTA: A three-dimensional visualization system for electronic and structural analysis, J. Appl. Cryst. **41**, 653 (2008).

[44] WaveMetrics, IGOR Pro, scientific data analysis software, URL: https://www.wavemetrics.com/products/igorpro/igorpro.htm.

[45] Mathworks, MATLAB, URL: https://www.mathworks.com/.

[46] Paul Scherrer Institute, Instrument dolly, https://www.psi.ch/smus/InstrumentDollyEN (2017).

[47] Paul Scherrer Institute, Gpd instrument page, https://www.psi.ch/en/smus/gpd (2017).

[48] Paul Scherrer Institute, Paul Scherrer Institute, https://www.psi.ch/en (2017).

[49] D. Scheuermann, Variox: Variable temperature cryostat, operator's handbook (2007), https://www.psi.ch/smus/InstrumentDollyEN/VARIOX.pdf .

[50] R. Khasanov, Z. Guguchia, A. Maisuradze, D. Andreica, M. Elender, A. Raselli, Z. Shermadini, T. Goko, F. Knecht, E. Morenzoni, *et al.*, High pressure research using muons at the Paul Scherrer Institute, High Press. Res. **36**, 140 (2016).

[51] D.-A. Andreica, Magnetic phase diagram in some Kondo-lattice compounds: Microscopic and macroscopic studies, Ph.D. thesis, ETH Zurich, 2001.

[52] JANIS ^{4}He vaporizer cryostat, quick references (2014), https://www.psi.ch/sites/default/files/import/smus/InstrumentGpdEN/QUICK_REF_Janis_version_May_2014.pdf.

[53] A. Suter and B. M. Wojek, MUSRFIT: A free platform-independent framework for μSR data analysis, Phys. Proc. **30**, 69 (2012).

[54] C. L. Bull, N. P. Funnell, M. G. Tucker, S. Hull, D. J. Francis, and W. G. Marshall, Pearl: The high pressure neutron powder diffractometer at ISIS, High Press. Res. **36**, 493 (2016).

[55] W. G. Marshall and D. J. Francis, Attainment of near-hydrostatic compression conditions using the Paris–Edinburgh cell, J. Appl. Cryst. **35**, 122 (2002).

[56] O. Arnold, J.-C. Bilheux, J. Borreguero, A. Buts, S. I. Campbell, L. Chapon, M. Doucet, N. Draper, R. F. Leal, M. Gigg, *et al.*, MANTID—Data analysis and visualization package for neutron scattering and μ SR experiments, Nucl. Instrum. Methods A **764**, 156 (2014).

[57] E. Arakawa, M. Ito, N. Ishimatsu, M. Suzuki, N. Kawamura, H. Sakurai, F. Itoh, Y. Honma, A. Ochiai, Y. Akahama, *et al.*, Experimental system for x-ray magnetic diffraction under extreme conditions, J. Phys. Chem. Solids **65**, 2089 (2004).

[58] N. Ishimatsu, N. Kawamura, M. Mizumaki, H. Maruyama, H. Sumiya, and T. Irifune, Applications of nano-polycrystalline diamond anvils to x-ray absorption spectroscopy under high pressure, High Press. Res. **36**, 381 (2016).

[59] T. Irifune, A. Kurio, S. Sakamoto, T. Inoue, and H. Sumiya, Ultrahard polycrystalline diamond from graphite, Nature (London) **421**, 599 (2003).

[60] N. Ishimatsu, K. Matsumoto, H. Maruyama, N. Kawamura, M. Mizumaki, H. Sumiya, and T. Irifune, Glitch-free x-ray absorption spectrum under high pressure obtained using

nano-polycrystalline diamond anvils, J. Synchr. Radiat. **19**, 768 (2012).

[61] B. Ravel and M. Newville, *ATHENA, ARTEMIS, HEPHAESTUS*: Data analysis for x-ray absorption spectroscopy using *IFEFFIT*, J. Synchr. Radiat. **12**, 537 (2005).

[62] J. Major, J. Mundy, M. Schmolz, A. Seeger, K.-P. Döring, K. Fürderer, M. Gladisch, D. Herlach, and G. Majer, Zero-field muon spin rotation in monocrystalline chromium, Hyperfine Interact. **31**, 259 (1986).

[63] A. Amato, R. Feyerherm, F. N. Gygax, A. Schenck, H. V. Löhneysen, and H. G. Schlager, Muon-spin-relaxation studies on the heavy-fermion system with non-Fermi-liquid behavior $CeCu_{5.9}Au_{0.1}$, Phys. Rev. B **52**, 54 (1995).

[64] A. Yaouanc and P. D. De Reotier, *Muon Spin Rotation, Relaxation, and Resonance: Applications to Condensed Matter* (Oxford University Press, Oxford, 2011), Vol. 147.

[65] J. Sugiyama, H. Nozaki, M. Harada, Y. Higuchi, H. Sakurai, E. J. Ansaldo, J. H. Brewer, L. Keller, V. Pomjakushin, and M. Månsson, Magnetic ground state of novel zigzag chain compounds, $NaCr_2O_4$ and $Ca_{1-x}Na_xCr_2O_4$, determined with muons and neutrons, Phys. Proc. **75**, 868 (2015).

[66] R. J. McQueeney, M. Yethiraj, S. Chang, W. Montfrooij, T. G. Perring, J. M. Honig, and P. Metcalf, Zener double exchange from local valence fluctuations in magnetite, Phys. Rev. Lett. **99**, 246401 (2007).

[67] T. Yamauchi, K. Hasegawa, H. Ueda, M. Isobe, and Y. Ueda, Competing electronic states under pressure in the double-exchange ferromagnetic peierls system $K_2Cr_8O_{16}$, Phys. Rev. B **92**, 165115 (2015).

[68] D. Li, K. Lee, B. Y. Wang, M. Osada, S. Crossley, H. R. Lee, Y. Cui, Y. Hikita, and H. Y. Hwang, Superconductivity in an infinite-layer nickelate, Nature (London) **572**, 624 (2019).

[69] E. Been, W.-S. Lee, H. Y. Hwang, Y. Cui, J. Zaanen, T. Devereaux, B. Moritz, and C. Jia, Electronic structure trends across the rare-earth series in superconducting infinite-layer nickelates, Phys. Rev. X **11**, 011050 (2021).

[70] M. Månsson, O. K. Forslund, Y. Sassa, E. Nocerino, J. Sugiyama, and N. Matsubara, Pressure dependent magnetic structure characterization of the Q1D compound $NaCr_2O_4$ (2019), iSIS experiment RB1910367; instrument PEARL; data format RAW/Nexus, https://data.isis.stfc.ac.uk/doi/STUDY/103216471/.